
Complex-Valued Autoencoders for Object Discovery

Sindy Löwe
UvA-Bosch Delta Lab
University of Amsterdam
loewe.sindy@gmail.com

Phillip Lippe
QUVA Lab
University of Amsterdam

Maja Rudolph
Bosch Center for AI

Max Welling
UvA-Bosch Delta Lab
University of Amsterdam

Abstract

Object-centric representations form the basis of human perception, and enable us to reason about the world and to systematically generalize to new settings. Currently, most works on unsupervised object discovery focus on slot-based approaches, which explicitly separate the latent representations of individual objects. While the result is easily interpretable, it usually requires the design of involved architectures. In contrast to this, we propose a comparatively simple approach – the Complex AutoEncoder (CAE) – that creates distributed object-centric representations. Following a coding scheme theorized to underlie object representations in biological neurons, its complex-valued activations represent two messages: their magnitudes express the presence of a feature, while the relative phase differences between neurons express which features should be bound together to create joint object representations. In contrast to previous approaches using complex-valued activations for object discovery, we present a fully unsupervised approach that is trained end-to-end – resulting in significant improvements in performance and efficiency on simple multi-object datasets. Further, we show that the CAE achieves competitive or better unsupervised object discovery performance compared to a state-of-the-art slot-based approach while being up to 100 times faster to train.

1 Introduction

Object discovery plays a crucial role in human perception and cognition (Wertheimer, 1922; Koffka, 1935; Köhler, 1967). It allows us to interact seamlessly with our environment, to reason about it, and to generalize systematically to new settings. To achieve this, our brain flexibly and dynamically combines information that is distributed across the network to represent and relate symbol-like entities, such as objects. The open question of how the brain implements these capabilities in a network of relatively fixed connections is known as the binding problem (Greff et al., 2020).

Currently, most work dedicated to solving the binding problem in machine learning focuses on slot-based approaches (Hinton et al., 2018; Burgess et al., 2019; Greff et al., 2019; Lin et al., 2020; Locatello et al., 2020; Kipf et al., 2022). Here, the latent representations are explicitly separated into “slots” which learn to represent different objects. These slots are highly interpretable; however, the introduction of a separate object-centric representation module in a model that otherwise does not exhibit object-centric features causes a number of problems. For one, it usually requires the design of involved architectures with iterative procedures, elaborate structural biases, and intricate training schemes to achieve a good separation of object features into slots. Moreover, this separation is often achieved by limiting the information flow and expressiveness of the model, leading to failure cases for

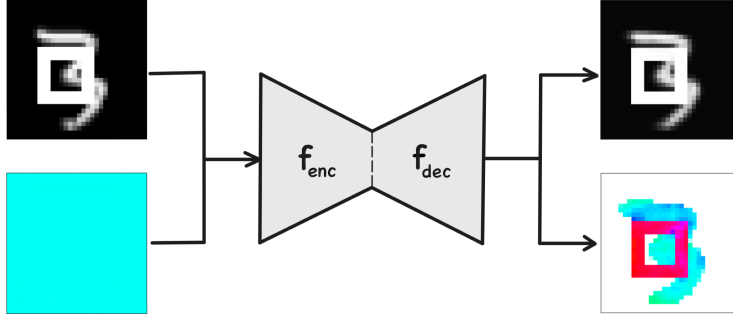


Figure 1: We propose the Complex AutoEncoder (CAE) – a simple and efficient object discovery approach leveraging complex-valued activations in an autoencoding architecture. Given a complex-valued input whose magnitude represents the input image (top left) and whose phase is set to a fixed value (bottom left), the model is trained to reconstruct the input image (top right), and learns to represent the disentangled object identities in its phase values without supervision (bottom right).

complex objects, e.g. with textured surfaces (Karazija et al., 2021). Finally, since all slots are created at the same level of representation, this approach cannot inherently represent part-whole hierarchies.

To overcome these issues of slot-based approaches, we take inspiration from the temporal correlation hypothesis from neuroscience (Singer & Gray, 1995; Singer, 2009) and design a model that learns representations of objects that are distributed across and embedded in the entire architecture. The temporal correlation hypothesis describes a coding scheme that biological neurons are theorized to use to overcome the binding problem. Essentially, it posits that each neuron sends two types of messages: (1) whether a certain feature is present or not, encoded by the discharge frequency or rate code, and (2) which other neurons to bind information to, encoded by the synchronicity of firing patterns.

Following Reichert & Serre (2014), we abstract away these two messages requiring binary spikes and temporal dynamics by making use of complex-valued activations in artificial neural networks. This allows each neuron to represent the presence of a feature through the complex number’s magnitude, and to bind this feature to other neurons’ features by aligning its phase value with theirs. After training a Deep Boltzmann Machine (DBM) with real-valued activations, Reichert & Serre (2014) apply this coding scheme at test-time to create object-centric representations. In our experiments, we show that this approach is slow to train due to its greedy layerwise training with Contrastive Divergence (Hinton, 2012), that it is slow to evaluate as it requires 100s-1000s of iterations to settle to an output configuration, and that it leads to unreliable results: even after training the DBM successfully as indicated by its reconstruction performance, its created phase values may not be representative of object identity.

To overcome these limitations of existing complex-valued approaches for object discovery, we propose a convolutional autoencoding architecture – the Complex AutoEncoder (CAE, Fig. 1) – that is trained end-to-end with complex-valued activations. First, we introduce several new, but simple, operations that enable each layer to learn to explicitly control the phase shift that it applies to its features. Then, we train the model in a fully unsupervised way by using a standard mean squared error between its real-valued input and the magnitudes of its complex-valued reconstructions. Interestingly, this simple setup suffices to reliably create phase values representative of object identity in the CAE. Our contributions are as follows:

- We propose the Complex AutoEncoder (CAE), a convolutional autoencoding architecture that takes inspiration from the neuroscientific temporal correlation hypothesis to create distributed object-centric features.
- We show that the CAE achieves competitive or better object discovery performance on simple multi-object datasets compared to SlotAttention (Locatello et al., 2020), a state-of-the-art slot-based approach, while being 10-100 times faster to train.
- We show that the CAE achieves significant improvements in performance and efficiency over the DBM approach proposed by Reichert & Serre (2014).

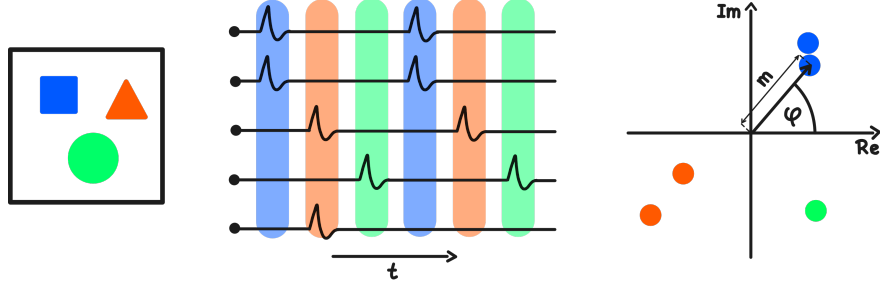


Figure 2: The temporal correlation hypothesis. **Left:** Input image with different objects. **Middle:** Implementation of the temporal correlation hypothesis with spiking neurons. Their spiking rate represents the presence of a feature, while their synchronization represents which features should be bound together to jointly represent an object. **Right:** Implementation of the temporal correlation hypothesis with complex-valued activations. Each complex number $z = m \cdot e^{i\varphi} \in \mathbb{C}$ is defined by its magnitude m and phase φ . This allows for an equivalent representation of feature presence and synchronization through the magnitude and phase values, respectively.

2 The Temporal Correlation Hypothesis

The Complex AutoEncoder takes inspiration from neuroscience, where the temporal correlation hypothesis describes a possible mechanism underlying object-centric representations in the brain. In this section, we will outline this hypothesis, and draw a connection to the complex-valued activations implemented in our proposed model.

In neuroscience, the binding problem describes the open question of how the brain binds information flexibly and dynamically within a network of fixed connectivity to give rise to coherent percepts, e.g. for different objects. Only by overcoming the binding problem, the brain is capable to represent all manner of objects, to attain a compositional understanding of the world, and to generalize robustly to new environments. While there is an ongoing debate as to their functional importance (Shadlen & Movshon, 1999; Ray & Maunsell, 2010), various works posit that the brain uses temporal dynamics to overcome the binding problem (Milner, 1974; Von Der Malsburg & Schneider, 1986; Singer & Gray, 1995; Engel et al., 1997; Singer, 1999; Fries, 2005; Singer, 2009; Palmigiano et al., 2017). Essentially, these theories postulate that the brain binds information from different neurons by synchronizing their firing patterns, while desynchronized firing represents information that ought to be processed separately. There are various manifestations of this theory; in this work, we will focus on the temporal correlation hypothesis (Singer & Gray, 1995; Singer, 2009).

The temporal correlation hypothesis describes how the oscillating behavior of biological neurons (a.k.a. brain waves) could be leveraged to overcome the binding problem. It posits that each neuron sends two messages through its spiking pattern (Fig. 2 - Middle): (1) The discharge frequency or rate code of a neuron encodes whether the feature that it is tuned to is present or not. The real-valued activation of neurons in artificial neural networks can be interpreted as the technical implementation of this message. (2) The relative timing between two neurons' spikes encodes whether the represented features of these neurons should be bound together or not. When firing in synchrony, the features they represent will be evaluated jointly by the target neuron and are thus combined in a flexible and dynamic way. Currently, very few works explore the use of this second message type in artificial neural networks.

In this paper, we take inspiration from the temporal correlation hypothesis to develop a machine learning approach capable of overcoming the binding problem. Inspired by previous work (Reichert & Serre, 2014), we abstract away from the spiking nature of biological neural networks and instead represent the two message types described above with the help of complex numbers (Fig. 2 - Right). As a result, we create an artificial neural network with complex-valued activations $z = m \cdot e^{i\varphi} \in \mathbb{C}$ in which the magnitude m can be interpreted as the rate code emitted by a spiking neuron (message (1) above) and the phase φ can be used as the mathematical mechanism to capture the temporal alignment of the firing patterns (message (2) above). In the next section, we describe how we implement this coding scheme.

3 Complex AutoEncoder

We propose the Complex AutoEncoder (CAE) – an object discovery model that leverages mechanisms inspired by the temporal correlation hypothesis to create distributed object-centric representations. We start by injecting complex-valued activations into a standard autoencoding architecture (Section 3.1). Ultimately, we want these complex-valued activations to convey two messages: their magnitudes should represent whether a feature is present, and their phase values should represent which features ought to be bound together. In Sections 3.2 and 3.3, we describe the setup of the model that gives rise to this coding scheme. Using the described mechanisms, after unsupervised training on a multi-object dataset, the CAE’s phase values represent different objects in a scene. In Section 3.4, we describe how we discretize these phase values to produce object-wise representations, as well as pixel-accurate segmentation masks for evaluation.

3.1 Complex-Valued Activations in Autoencoders

To enable an autoencoder to develop object-centric representations, we equip it with complex-valued activations. In this section, we will describe how we translate between the real-valued inputs and outputs used for training the model and the complex-valued activations used for representing object-centric features.

The Complex AutoEncoder (Fig. 1) takes a positive, real-valued input image $\mathbf{x} \in \mathbb{R}^+$ and associates each pixel with an initial phase $\varphi = 0 \in \mathbb{R}$ to create the complex-valued input \mathbf{x}' to the model:

$$\mathbf{x}' = \mathbf{x} \cdot e^{i\varphi} \in \mathbb{C} \quad (1)$$

The CAE applies a convolutional encoder f_{enc} and decoder f_{dec} with real-valued parameters $\theta \in \mathbb{R}$ to this complex-valued input to create a complex-valued reconstruction $\hat{\mathbf{z}} = f_{\text{dec}}(f_{\text{enc}}(\mathbf{x}'))$. To make use of existing deep learning frameworks, we do not apply layers to their complex-valued inputs directly. Instead, each layer extracts real-valued components (the real and imaginary part, or the magnitude and phase) from its input and processes them separately, before combining the results into a complex-valued output. We will describe this process in more detail in the following section.

We create the real-valued reconstruction $\hat{\mathbf{x}}$ by applying f_{out} , a 1×1 convolutional layer with a sigmoid activation function, on the magnitudes of the complex-valued output $\hat{\mathbf{z}}$ of the decoder: $\hat{\mathbf{x}} = f_{\text{out}}(|\hat{\mathbf{z}}|) \in \mathbb{R}^+$. This allows the model to learn an appropriate scaling and shift of the magnitudes to better match the input values. The model is trained by comparing this reconstruction to the original input using a mean squared error loss function $\mathcal{L} = \text{MSE}(\mathbf{x}, \hat{\mathbf{x}}) \in \mathbb{R}^+$ and by using the resulting gradients to update the model parameters.

Finally, we interpret the phase values $\varphi = \arg(\mathbf{z}) \in [0, 2\pi)$ of the complex-valued activations $\mathbf{z} \in \mathbb{C}$ as object assignments – either to extract object-wise representations from the latent space or to obtain a pixel-accurate segmentation mask in the output space. Here, $\arg(\mathbf{z})$ describes the angles between the positive real axis and the lines joining the origin and each element in \mathbf{z} .

3.2 Phase Alignment of Complex Numbers

For the CAE to accomplish good object discovery performance, the phases of activations representing the same object should be synchronized, while activations induced by different objects should be desynchronized. To achieve this, we need to enable the network to assign the same phases to some activations and different phases to others, and to precisely control phase shifts throughout the network. We achieve this by implementing the following three design principles in each network layer $f_{\theta} \in \{f_{\text{enc}}, f_{\text{dec}}\}$ parameterized by $\theta \in \mathbb{R}$ and applied to the input to that layer $\mathbf{z} \in \mathbb{C}$:

Synchronization First, we need to encourage the network to synchronize the phase values of features that should be bound together. This principle is fulfilled naturally when using additive operations between complex numbers: when adding two complex numbers of opposing phases, they suppress one another or even cancel one another out (a.k.a. destructive interference). Thus, to preserve features, the network needs to align their phase values (a.k.a. constructive interference).

Desynchronization Next, we need a mechanism that can desynchronize the phase values. Again, this is achieved naturally when using additive operations between complex numbers: when adding two complex numbers with a phase difference of 90° , for example, the result will lie in between these two

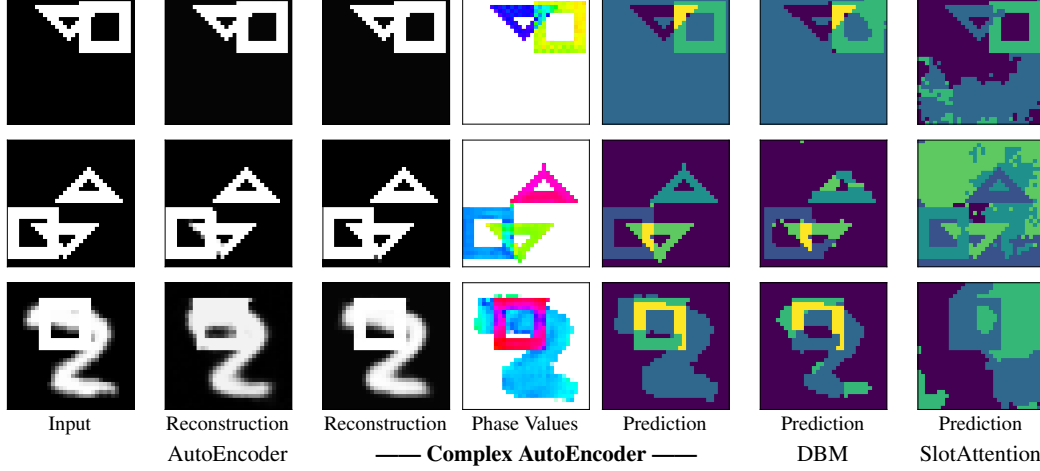


Figure 3: Visual comparison of the performance of the Complex AutoEncoder, a corresponding real-valued autoencoder, a DBM model and a SlotAttention model on random test-samples of the 2Shapes (**Top**), 3Shapes (**Middle**) and MNIST&Shape (**Bottom**) datasets. Areas in which objects overlap are removed before evaluation, resulting in yellow areas in the predictions of the CAE and the DBM model. The Complex AutoEncoder produces accurate reconstructions and object separations. Note, that the model assigns small magnitudes to the background, leading to white areas in the phase images and a clear foreground/background separation in the predictions.

numbers and thus be shifted, i.e. desynchronized by 45° . On top of this inherent mechanism, we add a second mechanism that lends the network more control over the precise phase shifts. Specifically, we first apply the weights $\mathbf{w} \in \theta$ of each layer separately to the real and imaginary components of its input:

$$\psi = f_{\mathbf{w}}(\mathbf{z}) = f_{\mathbf{w}}(\text{Re}(\mathbf{z}) + \text{Im}(\mathbf{z}) \cdot i) = f_{\mathbf{w}}(\text{Re}(\mathbf{z})) + f_{\mathbf{w}}(\text{Im}(\mathbf{z})) \cdot i \in \mathbb{C} \quad (2)$$

Then, we add separate biases $\mathbf{b}_m, \mathbf{b}_\varphi \in \theta$ to the magnitudes and phases of the resulting complex-valued representations ψ to create the intermediate magnitude \mathbf{m}_ψ and phase φ_ψ :

$$\mathbf{m}_\psi = |\psi| + \mathbf{b}_m \in \mathbb{R} \quad \varphi_\psi = \arg(\psi) + \mathbf{b}_\varphi \in \mathbb{R} \quad (3)$$

This formulation allows the model to influence the phase value of each activation directly through the bias \mathbf{b}_φ , and thus to learn explicit phase shifts throughout the network. Additionally, the bias \mathbf{b}_φ allows the model to break the symmetry created by the equal phase initialization (Eq. (1)).

Desynchronization vs. Inhibition Finally, we add a mechanism that enables the model to distinguish inhibitory inputs with aligned phases from excitatory inputs with opposing phases. To illustrate: given weights \mathbf{w} and activations \mathbf{a} , in the network formulation above it holds that $(-\mathbf{w}) \cdot \mathbf{a} = \mathbf{w} \cdot (-\mathbf{a})$. However, in our case, this is not desirable. To enable the model to learn meaningful phase shifts, it needs to be able to distinguish a negative weight from a negative activation, because one has an aligned phase and the other does not. Taking inspiration from Reichert & Serre (2014), we achieve this by taking the absolute value of the activations $(-\mathbf{w}) \cdot |\mathbf{a}| \neq \mathbf{w} \cdot |(-\mathbf{a})|$. Thus, we additionally apply each layer to the magnitude of its input and combine the result with \mathbf{m}_ψ to create the intermediate values \mathbf{m}_z :

$$\begin{aligned} \chi &= f_{\mathbf{w}}(|\mathbf{z}|) + \mathbf{b}_m \in \mathbb{R} \\ \mathbf{m}_z &= 0.5 \cdot \mathbf{m}_\psi + 0.5 \cdot \chi \in \mathbb{R} \end{aligned} \quad (4)$$

3.3 Complex-Valued Activation Function

We propose a new activation function for complex-valued activations to further ensure maximal control of the network over all phase shifts. To create a layer’s final output \mathbf{z}' , we apply a non-linearity on the intermediate values \mathbf{m}_z , but keep the phases φ_ψ unchanged:

$$\mathbf{z}' = \text{ReLU}(\text{BatchNorm}(\mathbf{m}_z)) \cdot e^{i\varphi_\psi} \in \mathbb{C} \quad (5)$$

Table 1: MSE and ARI scores (mean \pm standard error across 8 seeds) for the Complex AutoEncoder, its real-valued counterpart (AutoEncoder), a DBM model and a SlotAttention model in three simple multi-object datasets. The proposed Complex AutoEncoder achieves better reconstruction performance than its real-valued counterpart on all three datasets. Additionally, it significantly outperforms the DBM model across all three datasets, and its object discovery performance is competitive to SlotAttention on the 2Shapes and 3Shapes datasets. Finally, the CAE manages to disentangle the objects in the MNIST&Shape dataset, where both DBM and SlotAttention fail.

Dataset	Model	MSE \downarrow	ARI+BG \uparrow	ARI-BG \uparrow
2Shapes	Complex AutoEncoder	3.322e-04 \pm 1.583e-06	0.999 \pm 0.000	1.000 \pm 0.000
	AutoEncoder	5.565e-04 \pm 2.900e-04	—	—
	DBM	3.308e-03 \pm 1.024e-04	0.920 \pm 0.002	0.744 \pm 0.010
	SlotAttention	1.419e-04 \pm 1.410e-04*	0.812 \pm 0.081	1.000 \pm 0.000
3Shapes	Complex AutoEncoder	1.313e-04 \pm 2.020e-05	0.976 \pm 0.002	1.000 \pm 0.000
	AutoEncoder	8.568e-04 \pm 9.878e-05	—	—
	DBM	1.045e-02 \pm 1.494e-04	0.856 \pm 0.006	0.419 \pm 0.023
	SlotAttention	1.827e-04 \pm 3.125e-05*	0.107 \pm 0.008	0.997 \pm 0.001
MNIST&Shape	Complex AutoEncoder	3.185e-03 \pm 1.514e-04	0.783 \pm 0.004	0.971 \pm 0.011
	AutoEncoder	5.792e-03 \pm 5.553e-04	—	—
	DBM	1.560e-02 \pm 8.069e-05*	0.718 \pm 0.002	0.175 \pm 0.006
	SlotAttention	5.438e-03 \pm 1.607e-04*	0.047 \pm 0.013	0.089 \pm 0.028

*The grayed-out performances are not comparable due to the use of different autoencoding setups.

There are several things to note in this setup. First, \mathbf{m}_z might contain negative values as a result of the summation with potentially negative values in the magnitude bias \mathbf{b}_m (Eq. (3)), as well as potentially negative values in χ (Eq. (4)). Nonetheless, it is biased to be positive due to the usage of absolute values throughout each layer. Second, by applying BatchNormalization (Ioffe & Szegedy, 2015), we ensure that – at least initially – \mathbf{m}_z becomes zero-centered and therefore makes use of the non-linear part of the ReLU activation function (Krizhevsky et al., 2012). At the same time, BatchNormalization provides the flexibility to learn to shift and scale these values if appropriate. Finally, the ReLU non-linearity ensures that the magnitude of \mathbf{z}' is positive and thus prevents any phase flips.

3.4 Creating Discrete Object Assignments from Continuous Phase Values

To extract object-wise representations from the latent space, as well as pixel-accurate segmentation masks from the output space, we create discrete object assignments for each feature by applying a clustering procedure to the phase values. We start this clustering procedure with two pre-processing steps. First, we account for the circular nature of the phase values by mapping them onto a unit circle. This prevents values close to 0 and 2π from being assigned to different clusters despite representing similar angles. Then, to account for the fact that the phase values of complex numbers with small magnitudes become increasingly random, we scale features by a factor of $10 \cdot m$ if their corresponding magnitude $m < 0.1$. As a result of this scaling, these features will fall within the unit circle, close to the origin. In our experiments, we find that they tend to be assigned their own cluster and usually represent the background. Finally, we apply k -means, with k corresponding to the number of objects in the input plus one for the background, and interpret the resulting cluster assignment for each phase value as the predicted object assignment of the corresponding feature.

Note that this discretization of object assignments is only required for the evaluation of the CAE. During training, the CAE learns continuous object assignments through its phase values and therefore does not require k to be set in advance.

4 Results

In this section, we evaluate whether the Complex AutoEncoder can learn to create meaningful phase separations representing different objects in an unsupervised way. We will first describe the general setup of our experiments, before investigating the results across three simple multi-object datasets.

4.1 Setup

Datasets We evaluate the Complex AutoEncoder on three grayscale datasets: 2Shapes, 3Shapes, and MNIST&Shape. For each of these datasets, we generate 50,000 training images and 10,000 images for validation and testing, respectively. All images contain 32×32 pixels. The 2Shapes dataset represents the easiest setting, with two randomly placed objects (\square, \triangle) in each image. The 3Shapes dataset contains a third randomly placed object (∇) per image. This creates a slightly more complex setting due to the higher object count, the two similar shapes (\triangle, ∇), and stronger overlap between objects. Finally, the MNIST&Shape dataset combines an MNIST digit (LeCun et al., 2010) and a randomly placed shape (\square or ∇) in each image. This creates a challenging setting with more diverse objects. Finally, for evaluation, we generate pixel-accurate segmentation masks for all images. More details in Appendix A.4.

Model & Training We make use of a fairly standard convolutional autoencoder architecture, as presented in Lippe (2021) (details in Appendix A.1). We train the model using Adam (Kingma & Ba, 2015) and a batch-size of 64 for 10,000 – 100,000 steps depending on the dataset. Within the first 500 steps of training, we linearly warm up the learning rate (Goyal et al., 2017) to its final value of $1e-3$. All experiments are implemented in PyTorch 1.10 (Paszke et al., 2019) and were run on a single Nvidia GTX 1080Ti. To ensure the comparability of runtimes between models, all experiments were run on the same machine and with the same underlying implementations for data-loading, training and evaluation wherever possible.

Baselines We compare the CAE to three baseline models. First, we compare it against a Deep Boltzmann Machine (DBM; Salakhutdinov & Hinton (2009)) that closely follows Reichert & Serre (2014). We test two architectures for this model, one resembling the setup of the CAE (6-layer DBM) and one following the architecture used by Reichert & Serre (2014) (3-layer DBM), and report the results of the best performing model for each dataset. For a full breakdown of all results, see Appendix B.1. Additionally, we provide an in-depth discussion on the limitations of our re-implementation in Appendix A.2. The second baseline we consider is a state-of-the-art slot-based approach: SlotAttention (Locatello et al., 2020). SlotAttention is an iterative attention mechanism that produces k slots which learn to represent individual objects in the input, and has achieved impressive unsupervised object discovery results on synthetic multi-object datasets. For more details, see Appendix A.3. Finally, we compare the CAE against a corresponding real-valued autoencoder. This model uses the same general architecture and training procedure as the CAE, but does not employ complex-valued activations or any of the mechanisms described in Section 3.2. It does, however, apply BatchNormalization before each ReLU as we have found that this improves performance in the real domain as well.

Metrics We use three metrics to evaluate the performance of the CAE and to compare it with the baselines. We measure the reconstruction performance in terms of mean squared error (MSE). To assess the object discovery performance, we compute Adjusted Rand Index (ARI) scores (Rand, 1971; Hubert & Arabie, 1985). ARI measures clustering similarity, where a score of 0 indicates chance level and a score of 1 indicates a perfect match. We utilize this metric in two ways. First, following previous work (Greff et al., 2019; Locatello et al., 2020), we evaluate “ARI-BG” where we exclude the background labels from the evaluation. Additionally, we assess “ARI+BG” which evaluates the performance on all pixels. For both ARI scores, we remove areas in which objects overlap from the evaluation, as they are ambiguous in the grayscale setting.

4.2 Evaluation

First, we compare the quantitative performance of the CAE against the three baselines in Table 1.

Object Discovery Performance The *Complex AutoEncoder* achieves considerably better object discovery performance than the *DBM* model across all three tested datasets. In fact, we find that our re-implementation of the DBM model only achieves consistent object separation in the simplest 2Shapes dataset, and largely fails on the other two – despite achieving a reasonable reconstruction performance on all datasets (see Fig. 6 in the Appendix). When comparing the object discovery performance of the CAE against *SlotAttention*, we make three observations: (1) Both models achieve (near) perfect ARI-BG scores on the 2Shapes and 3Shapes datasets. (2) On all datasets, the CAE achieves considerably better ARI+BG scores indicating a more accurate separation of foreground and background. (3) On the MNIST&Shape dataset, the CAE achieves an almost perfect ARI-BG score,

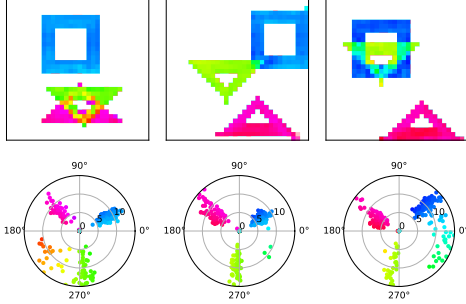


Figure 4: Phase separation in the CAE. **Top:** Output phase images. **Bottom:** Plotting every output value in the complex plane and applying the same color coding as above. The phases of the three objects are almost maximally misaligned. Interestingly, areas in which the objects overlap get assigned intermediate phase values.

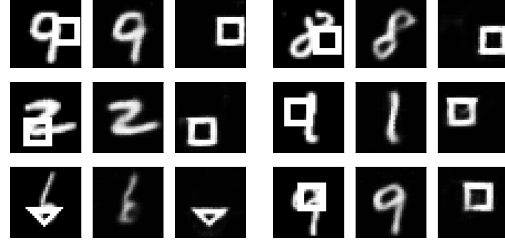


Figure 5: Investigating object-centricity of the latent features in the CAE. Columns 1 & 4: input images. Columns 2-3 & 5-6: object-wise reconstructions. By clustering features created by the encoder according to their phase values, we can extract representations of the individual objects and reconstruct them separately.

while SlotAttention’s performance is close to chance level. Overall, this shows that the Complex AutoEncoder achieves strong object discovery performance. On top of this, despite its simple and efficient design, it can overcome the challenges set by the MNIST&Shape dataset (high diversity in object shapes and relatively large object sizes), while neither the DBM model nor SlotAttention can.

Reconstruction Performance The *Complex AutoEncoder* creates more accurate reconstructions than its real-valued counterpart (*AutoEncoder*) on all three multi-object datasets. This illustrates that the CAE uses its complex-valued activations to create a better disentanglement of object features.

Object-Centric Representations To evaluate whether the CAE creates object-centric representations throughout the model, we cluster the latent features created by the encoder (Section 3.4), and fine-tune the decoder to reconstruct separate objects from the individual clusters. As shown in Fig. 5, this allows us to create accurate reconstructions of the individual objects, indicating that the phase values are representative of object affiliation throughout the model.

Qualitative Evaluation In Fig. 3, we show exemplary outputs of the four compared models for each dataset (for more results, see Appendix B.4). When looking more closely at the phase separation created by the Complex AutoEncoder as shown in Fig. 4, we find that it assigns almost maximally distant phase values to the different objects. Interestingly, the phase values of overlapping areas tend to fall in between the phase values of the individual objects. Since it is ambiguous in the 3Shapes dataset, which object is in the foreground and which one is in the background, this shows that the model accurately expresses the uncertainty that it encounters in these overlapping areas.

Sensitivity Analysis We evaluate the influence of certain design decisions on the performance of the Complex AutoEncoder in Table 2. We find that there are several crucial components contributing to the CAE’s ability to achieve meaningful phase separation without supervision: the introduction of a separate bias term b_φ that is applied to the phase values of each layer (Eq. (3)); the χ term (Eq. (4)) that ensures that desynchronized inputs influence a layer’s output differently from inhibitive ones; our proposed activation function for complex-valued features that combines a ReLU non-linearity with BatchNormalization (Eq. (5)); and the use of real-valued weights instead of complex-

Table 2: Sensitivity Analysis on the 2Shapes dataset (mean \pm standard error across 8 seeds). We find that there are several crucial components contributing to the CAE’s ability to achieve meaningful phase separation without supervision.

Name	MSE	ARI-BG
Complex AutoEncoder	$3.322\text{e-}04 \pm 1.583\text{e-}06$	1.000 ± 0.000
$-f_{\text{out}}$	$2.462\text{e-}03 \pm 1.458\text{e-}03$	0.939 ± 0.039
$-b_\varphi$	$5.127\text{e-}04 \pm 6.793\text{e-}05$	0.100 ± 0.035
$-\chi$	$3.227\text{e-}03 \pm 5.013\text{e-}04$	0.074 ± 0.068
BatchNorm	$6.165\text{e-}02 \pm 2.228\text{e-}02$	0.373 ± 0.137
Sigmoid non-linearity	$6.488\text{e-}03 \pm 4.547\text{e-}04$	0.117 ± 0.052
Complex Weights	$5.465\text{e-}04 \pm 8.980\text{e-}05$	0.122 ± 0.101

valued ones. Additionally, we find that the final 1×1 convolutional layer f_{out} that creates the real-valued reconstructions from the magnitudes of the complex-valued outputs improves the model’s performance. Finally, we observe that the bottleneck size has relatively little influence on the performance of the Complex AutoEncoder (Fig. 8 in the Appendix). This indicates that the CAE does need to restrict the expressivity of the model to create disentangled object representations.

Runtime Due to its non-iterative design and its end-to-end optimization with comparatively few training steps, the CAE is between 1.1 and 21.0 times faster to train than the DBM model, and between 10.0 and 99.8 times faster than SlotAttention. The precise values depend on the dataset and DBM architecture used. On the 2Shapes dataset, for example, the CAE is 2.1 times faster to train than the DBM model and 99.8 times faster than SlotAttention. Besides this, we find that the discretization of phase values with k -means leads to significantly slower evaluation times for both the CAE and DBM. As a result, the CAE is approximately 10 times slower to evaluate than SlotAttention. The DBM is slowed down even further by its iterative settling procedure, leading to 2.0 - 16.6 times slower evaluation times compared to the CAE. See Appendix B.2 for a detailed breakdown of all runtimes.

5 Related Work

Object Discovery There is a broad range of approaches attempting to solve the binding problem in artificial neural networks (see Greff et al. (2020) for a great overview). However, most works focus on one particular representational format for objects: slots. These slots create an explicit separation of the latent representations for different objects. Additionally, they create an explicit separation between a specialized object-centric representation part of the model and non-object-centric parts that merely support the former, for example, through encoding and decoding functionality. In contrast to this, the Complex AutoEncoder embeds object-centricity into the entire architecture and creates distributed object-centric representations.

To create slot-based object-centric representations, different mechanisms have been proposed to overcome the binding problem, i.e. to break the symmetry between the representations of different objects in a network of fixed weights. One way to break this symmetry is to enforce an order along a certain axis. This can be achieved by imposing an order on the slots (Eslami et al., 2016; Burgess et al., 2019; Engelcke et al., 2020), by assigning slots to particular spatial coordinates (Santoro et al., 2017; Lin et al., 2020), or by learning specialized slots for different object types (Hinton et al., 2011, 2018). Approaches that create the most general slot representations do not enforce any such order, but require iterative procedures to break the symmetries instead (Greff et al., 2019; Goyal et al., 2021). SlotAttention (Locatello et al., 2020; Kipf et al., 2022), which falls into this final category, breaks the symmetry between slots through an iterative attention mechanism. It was recently shown to also perform well on more realistic textured video datasets in a weakly-supervised setting (Kipf et al., 2022).

Object Discovery with Complex-Valued Networks A variety of research has explored different activation functions, training regimes, and applications for complex-valued neural networks (see Bassey et al. (2021) for a review). Despite this, there has been little research on the use of complex-valued networks for object discovery. The earliest works in this direction are by Mozer et al. (1992); Zemel et al. (1995). Their architectures learn to assign different phase values to different objects through a supervised training procedure. Rao et al. (2008); Rao & Cecchi (2010, 2011) enable their complex-valued neural networks to separate overlapping objects on test images by training them on images of individual objects of the same type. Finally, the only existing complex-valued network for object discovery that is fully unsupervised was developed by Reichert & Serre (2014). They train a real-valued Deep Boltzmann Machine on datasets similar to the ones presented here. At test time, they inject complex-valued activations to create phases representative of object identity.

All these methods initialize the complex-valued inputs to their networks with the magnitudes of the input images and with random phase values. As a result, they require iterative procedures with 10s-1000s of iterations to settle to an output configuration. In contrast to that, the proposed Complex AutoEncoder initializes all phase values with a fixed value and – after fully unsupervised, end-to-end training with complex-valued activations – only requires a single forward-pass through the model. This greatly improves the efficiency and performance of complex-valued neural networks for object discovery.

6 Conclusion

Summary We present the Complex AutoEncoder – an object discovery approach that takes inspiration from neuroscience to implement distributed object-centric representations. After introducing complex-valued activations into a convolutional autoencoder, it learns to encode feature information in the activations’ magnitudes and object affiliation in their phase values. We show that this simple and fully unsupervised setup suffices to achieve strong object discovery results on simple multi-object datasets while being fast to train.

Limitations and Future Work The proposed Complex AutoEncoder constitutes a first step towards efficient distributed object-centric representation learning, but some limitations remain. Most importantly, due to the limited range of the phase values, object discovery approaches using complex-valued activations can only represent a small number of objects at a time. Additionally, we find that the phase values of different objects are interdependent and thus require the same set of objects or object-types to be present in each image to create reliable phase separations. Finally, it remains unclear how complex-valued networks for object discovery could be applied to RGB images. These restrictions currently prevent these approaches from being applied to more complex multi-object datasets. Nonetheless, the Complex AutoEncoder provides an important step forward by proposing a simple and efficient non-iterative design, that, for the first time, was shown to achieve competitive results to a slot-based approach in simple multi-object datasets. It remains an intriguing direction for future research to overcome the limitations described above and to uncover the full potential of distributed object-centric representation learning approaches.

Acknowledgements

We thank David P. Reichert and Thomas Serre for their helpful guidance for re-implementing their proposed DBM model. Additionally, we thank Emiel Hoozeboom, T. Anderson Keller, and Joop Pascha for their valuable feedback on the manuscript.

References

- Jimmy Lei Ba, Jamie Ryan Kiros, and Geoffrey E Hinton. Layer normalization. *arXiv preprint arXiv:1607.06450*, 2016.
- Joshua Basse, Lijun Qian, and Xianfang Li. A survey of complex-valued neural networks. *arXiv preprint arXiv:2101.12249*, 2021.
- Christopher P Burgess, Loic Matthey, Nicholas Watters, Rishabh Kabra, Irina Higgins, Matt Botvinick, and Alexander Lerchner. MONet: Unsupervised scene decomposition and representation. *arXiv preprint arXiv:1901.11390*, 2019.
- Andreas K Engel, Pieter R Roelfsema, Pascal Fries, Michael Brecht, and Wolf Singer. Role of the temporal domain for response selection and perceptual binding. *Cerebral Cortex (New York, NY: 1991)*, 7(6):571–582, 1997.
- Martin Engelcke, Adam R Kosior, Oivi Parker Jones, and Ingmar Posner. GENESIS: Generative scene inference and sampling with object-centric latent representations. *International Conference on Learning Representations (ICLR)*, 2020.
- SM Ali Eslami, Nicolas Heess, Theophane Weber, Yuval Tassa, David Szepesvari, Geoffrey E Hinton, et al. Attend, infer, repeat: Fast scene understanding with generative models. In *Advances in Neural Information Processing Systems*, pp. 3225–3233, 2016.
- Pascal Fries. A mechanism for cognitive dynamics: neuronal communication through neuronal coherence. *Trends in Cognitive Sciences*, 9(10):474–480, 2005.
- Anirudh Goyal, Alex Lamb, Jordan Hoffmann, Shagun Sodhani, Sergey Levine, Yoshua Bengio, and Bernhard Schölkopf. Recurrent independent mechanisms. *International Conference on Learning Representations (ICLR)*, 2021.
- Priya Goyal, Piotr Dollár, Ross Girshick, Pieter Noordhuis, Lukasz Wesolowski, Aapo Kyrola, Andrew Tulloch, Yangqing Jia, and Kaiming He. Accurate, large minibatch SGD: Training imagenet in 1 hour. *arXiv preprint arXiv:1706.02677*, 2017.

- Klaus Greff, Raphaël Lopez Kaufman, Rishabh Kabra, Nick Watters, Christopher Burgess, Daniel Zoran, Loic Matthey, Matthew Botvinick, and Alexander Lerchner. Multi-object representation learning with iterative variational inference. In *International Conference on Machine Learning (ICML)*, pp. 2424–2433, 2019.
- Klaus Greff, Sjoerd van Steenkiste, and Jürgen Schmidhuber. On the binding problem in artificial neural networks. *arXiv preprint arXiv:2012.05208*, 2020.
- Geoffrey E Hinton. A practical guide to training restricted boltzmann machines. In *Neural Networks: Tricks of the Trade*, pp. 599–619. Springer, 2012.
- Geoffrey E Hinton, Alex Krizhevsky, and Sida D Wang. Transforming auto-encoders. In *International Conference on Artificial Neural Networks*, pp. 44–51. Springer, 2011.
- Geoffrey E Hinton, Sara Sabour, and Nicholas Frosst. Matrix capsules with em routing. In *International Conference on Learning Representations (ICLR)*, 2018.
- Lawrence Hubert and Phipps Arabie. Comparing partitions. *Journal of Classification*, 2(1):193–218, 1985.
- Sergey Ioffe and Christian Szegedy. Batch normalization: Accelerating deep network training by reducing internal covariate shift. In *International Conference on Machine Learning (ICML)*, pp. 448–456, 2015.
- Laurynas Karazija, Iro Laina, and Christian Rupprecht. Clevrtex: A texture-rich benchmark for unsupervised multi-object segmentation. In *Thirty-fifth Conference on Neural Information Processing Systems Datasets and Benchmarks Track (Round 2)*, 2021.
- Diederik P Kingma and Jimmy Ba. Adam: A method for stochastic optimization. *International Conference on Learning Representations (ICLR)*, 2015.
- Thomas Kipf, Gamaleldin F Elsayed, Aravindh Mahendran, Austin Stone, Sara Sabour, Georg Heigold, Rico Jonschkowski, Alexey Dosovitskiy, and Klaus Greff. Conditional object-centric learning from video. *International Conference on Learning Representations (ICLR)*, 2022.
- Kurt Koffka. Principles of gestalt psychology. *Philosophy and Scientific Method*, 32(8), 1935.
- Wolfgang Köhler. Gestalt psychology. *Psychologische Forschung*, 31(1):XVIII–XXX, 1967.
- Alex Krizhevsky, Ilya Sutskever, and Geoffrey E Hinton. Imagenet classification with deep convolutional neural networks. *Advances in Neural Information Processing Systems*, 25, 2012.
- Yann LeCun, Corinna Cortes, and CJ Burges. Mnist handwritten digit database. *ATT Labs [Online]*. Available: <http://yann.lecun.com/exdb/mnist>, 2, 2010.
- Zhixuan Lin, Yi-Fu Wu, Skand Vishwanath Peri, Weihao Sun, Gautam Singh, Fei Deng, Jindong Jiang, and Sungjin Ahn. SPACE: Unsupervised object-oriented scene representation via spatial attention and decomposition. *International Conference on Learning Representations (ICLR)*, 2020.
- Phillip Lippe. UvA Deep Learning Tutorials, 2021. URL uvadlc-notebooks.readthedocs.io.
- Francesco Locatello, Dirk Weissenborn, Thomas Unterthiner, Aravindh Mahendran, Georg Heigold, Jakob Uszkoreit, Alexey Dosovitskiy, and Thomas Kipf. Object-centric learning with slot attention. *Advances in Neural Information Processing Systems*, 2020.
- Peter M Milner. A model for visual shape recognition. *Psychological Review*, 81(6):521, 1974.
- Michael C Mozer, Richard S Zemel, Marlene Behrmann, and Christopher KI Williams. Learning to segment images using dynamic feature binding. *Neural Computation*, 4(5):650–665, 1992.
- Agostina Palmigiano, Theo Geisel, Fred Wolf, and Demian Battaglia. Flexible information routing by transient synchrony. *Nature Neuroscience*, 20(7):1014–1022, 2017.
- Adam Paszke, Sam Gross, Francisco Massa, Adam Lerer, James Bradbury, Gregory Chanan, Trevor Killeen, Zeming Lin, Natalia Gimelshein, Luca Antiga, Alban Desmaison, Andreas Kopf, Edward Yang, Zachary DeVito, Martin Raison, Alykhan Tejani, Sasank Chilamkurthy, Benoit Steiner, Lu Fang, Junjie Bai, and Soumith Chintala. Pytorch: An imperative style, high-performance deep learning library. *Advances in Neural Information Processing Systems* 32, pp. 8024–8035, 2019.
- William M Rand. Objective criteria for the evaluation of clustering methods. *Journal of the American Statistical Association*, 66(336):846–850, 1971.

- A Ravishankar Rao and Guillermo A Cecchi. An objective function utilizing complex sparsity for efficient segmentation in multi-layer oscillatory networks. *International Journal of Intelligent Computing and Cybernetics*, 2010.
- A Ravishankar Rao and Guillermo A Cecchi. The effects of feedback and lateral connections on perceptual processing: A study using oscillatory networks. In *The 2011 International Joint Conference on Neural Networks*, pp. 1177–1184. IEEE, 2011.
- A Ravishankar Rao, Guillermo A Cecchi, Charles C Peck, and James R Kozloski. Unsupervised segmentation with dynamical units. *IEEE Transactions on Neural Networks*, 19(1):168–182, 2008.
- Supratim Ray and John HR Maunsell. Differences in gamma frequencies across visual cortex restrict their possible use in computation. *Neuron*, 67(5):885–896, 2010.
- David P Reichert and Thomas Serre. Neuronal synchrony in complex-valued deep networks. *International Conference on Learning Representations (ICLR)*, 2014.
- Ruslan Salakhutdinov and Geoffrey Hinton. Deep boltzmann machines. In *Proceedings of the Twelfth International Conference on Artificial Intelligence and Statistics*, volume 5, pp. 448–455. PMLR, 2009.
- Adam Santoro, David Raposo, David G Barrett, Mateusz Malinowski, Razvan Pascanu, Peter Battaglia, and Timothy Lillicrap. A simple neural network module for relational reasoning. In *Advances in Neural Information Processing Systems*, pp. 4967–4976, 2017.
- Michael N Shadlen and J Anthony Movshon. Synchrony unbound: review a critical evaluation of the temporal binding hypothesis. *Neuron*, 24:67–77, 1999.
- Wolf Singer. Neuronal synchrony: a versatile code for the definition of relations? *Neuron*, 24(1):49–65, 1999.
- Wolf Singer. Distributed processing and temporal codes in neuronal networks. *Cognitive Neurodynamics*, 3(3):189–196, 2009.
- Wolf Singer and Charles M Gray. Visual feature integration and the temporal correlation hypothesis. *Annual Review of Neuroscience*, 18(1):555–586, 1995.
- Tijmen Tieleman. Training restricted boltzmann machines using approximations to the likelihood gradient. In *International Conference on Machine Learning (ICML)*, pp. 1064–1071, 2008.
- Christoph Von Der Malsburg and Werner Schneider. A neural cocktail-party processor. *Biological Cybernetics*, 54(1):29–40, 1986.
- Max Wertheimer. Untersuchungen zur Lehre von der Gestalt. *Psychologische Forschung*, 1(1):47–58, 1922.
- Richard S Zemel, Christopher KI Williams, and Michael C Mozer. Lending direction to neural networks. *Neural Networks*, 8(4):503–512, 1995.

Appendix

Complex-Valued Autoencoders for Object Discovery

A Experimental Details

A.1 (Complex) AutoEncoder

Table 3 shows the architecture of the Complex AutoEncoder, as well as its real-valued counterpart. We used the default parameter initialization of PyTorch for all layers, except f_{out} for which we set the initial weight $w = 1$ and the initial bias $b = 0$. Additionally, we initialize all phase-biases b_{φ} with zero. After the linear layers, we apply Layer Normalization (Ba et al., 2016) instead of Batch Normalization.

Table 3: Autoencoding architecture used for the Complex AutoEncoder, as well as the real-valued autoencoder baseline.

	Layer	Feature Dimension (H × W × C)	Kernel	Stride	Padding Input / Output	Activation Function
f_{enc}	Conv	$16 \times 16 \times 32$	3	2	1 / 0	(Complex-)ReLU
	Conv	$16 \times 16 \times 32$	3	1	1 / 0	(Complex-)ReLU
	Conv	$8 \times 8 \times 64$	3	2	1 / 0	(Complex-)ReLU
	Conv	$8 \times 8 \times 64$	3	1	1 / 0	(Complex-)ReLU
	Conv	$4 \times 4 \times 64$	3	2	1 / 0	(Complex-)ReLU
	Reshape	$1 \times 1 \times 1024$	-	-	-	-
	Linear	$1 \times 1 \times 64$	-	-	-	(Complex-)ReLU
f_{dec}	Linear	$1 \times 1 \times 1024$	-	-	-	(Complex-)ReLU
	Reshape	$4 \times 4 \times 64$	-	-	-	-
	TransConv	$8 \times 8 \times 64$	3	2	1 / 1	(Complex-)ReLU
	Conv	$8 \times 8 \times 64$	3	1	1 / 0	(Complex-)ReLU
	TransConv	$16 \times 16 \times 32$	3	2	1 / 1	(Complex-)ReLU
	Conv	$16 \times 16 \times 32$	3	1	1 / 0	(Complex-)ReLU
	TransConv	$32 \times 32 \times 1$	3	2	1 / 1	(Complex-)ReLU

We optimized all hyperparameters, except the number of training steps, on the validation set of the 3Shapes dataset and subsequently applied them for the training on all datasets. Across the board, we found that each hyperparameter setting that improved the performance of the Complex AutoEncoder also improved the performance of the real-valued autoencoder and vice versa. As a result, we use the same hyperparameters to train both models.

To create the object-wise reconstructions in Fig. 5, we first cluster the features created by the encoder f_{enc} by following the procedure described in Section 3.4. Then, we mask out all values that are not part of a particular cluster with zeros. Finally, we fine-tune the decoder to reconstruct individual objects given these masked out feature vectors for 10,000 steps using Adam with a learning rate of $5e-5$.

A.2 DBM

In this section, we will first discuss the limitations of our re-implementation, then outline our final experimental setting, and finally list all other setups that we considered.

Limitations of our Re-Implementation To implement the Deep Boltzmann Machine (DBM) model, we closely followed the descriptions in Reichert & Serre (2014). However, due to the lack of a publicly available codebase, some aspects of the implementation remained unclear, and we used private communication with the authors, as well as extensive experimentation to fill in the gaps. Despite the considerable effort that we put into reproducing their results – involving more fine-tuning

than we performed for the proposed CAE model – our implementation seems to perform worse than the original implementation, as indicated by the visual comparison in Fig. 6. We note two things about this comparison: (1) Since Reichert & Serre (2014) report stability issues for their implementation and state that they only show results of the “well performing networks”, we accordingly chose the seed with the best performance in our implementation to create the samples for the qualitative comparison. (2) We can not quantify the observed performance gap, as Reichert & Serre (2014) do not provide quantitative results in their paper.

Independent of the implementation, the DBM model is less efficient than the CAE by design, due to its greedy layerwise training with Contrastive Divergence that requires a comparatively large number of training steps, and the iterative settling procedure used for evaluation.

Final Setup We implement all layers as fully-connected layers with a potentially restricted receptive field as proposed by Reichert & Serre (2014). To achieve this, we mask out all weights outside the receptive field with zero. This results in a setup that resembles a convolutional layer without shared weights. Additionally, we apply a separate bias to each spatial location. We implement these layers in two different architectures. First, we closely followed the model description provided by Reichert & Serre (2014) and use a three-layer architecture (3-layer DBM). The layers in this architecture have a receptive field size in [height, width] of [7, 7], [7, 7] and [20, 20] (i.e. global), and hidden dimensions in [height, width, channel] or [channel] of [26, 26, 3], [20, 20, 5], and [676], respectively. As a second architecture, we test a DBM whose layers resemble the setup of the encoder f_{enc} of the (Complex) AutoEncoder (6-layer DBM, Table 3). Instead of convolutional layers, we use the fully-connected layers with restricted receptive field sizes as described above, where the kernel size corresponds to the receptive field size. Note that even though this setup resembles that of the CAE, its parameter count differs considerably as weights are not shared across locations, but they are shared for the forward and backward pass (i.e. encoding and decoding). For all layers in both models, we use a sigmoid non-linearity as activation function.

We train each layer greedily as a separate Restricted Boltzmann Machine (RBM) using 1-step Contrastive Divergence (Hinton, 2012) with a learning rate of $1e-1$, momentum coefficient of 0.5 and weight-decay factor of $1e-4$, for 50,000 and 100,000 steps. After training, to create object-centric representations, we inject complex-valued activations into the model. To do so, we use the input images as magnitudes, randomly sample phase values for each pixel from $\mathcal{U}(0, 2\pi)$ and initialize the hidden state of each layer with an initial forward pass. Then, clamping the magnitudes of the visible units to the input images, we iterate the complex-valued activations 500 times through the model. To evaluate the resulting phase values, we use the same discretization procedure as for the CAE (see Section 3.4). This procedure includes a step in which small magnitudes are used to mask out their corresponding phase values. Since we use the final output of the DBM to extract both the phases and magnitudes, and not some intermediate values as in the CAE, this model creates a good foreground-background separation by relying explicitly on a black background – resulting in small magnitudes for the reconstruction and thus masked out phases. Thus, the ARI+BG performance of the DBM models is negligible, as it depends directly on its reconstruction performance.

Finally, since the DBM is only well-defined on binary inputs, we apply this model to a binarized version of the MNIST&Shape dataset. To create this version of the dataset, we use the same threshold as for the creation of the pixel-wise labels (-0.8 after normalization to the [-1,1] range, see Appendix A.4) to decide whether a pixel is assigned a “0” or “1” value.

Tested Setups Besides this final setup which achieved the best validation performance, we have tried a wide range of other experimental settings:

- We trained the 3-layer DBM model for up to 1,500,000 steps. Interestingly, even though the reconstruction performance keeps on improving, object discovery performance worsens (similarly to the effects observed in Table 5).
- We tested different learning rates [$1, 1e-1, 1e-2, 1e-3, 1e-4$] and different momentum terms [0.5, 1].
- We implemented and tested 5-step persistent contrastive divergence (Tieleman, 2008), an alternative training algorithm for RBMs which was shown to achieve better results, with different learning rates, momentum terms and learning rate schedules (fixed and exponential decay).
- We tried to share the weights and biases across spatial locations to create layers that resemble a convolutional layer more closely.



Figure 6: Qualitative comparison between random samples from the best performing seed of our re-implementation of the DBM model in Reichert & Serre (2014) (**left**) and original samples taken from their paper on slightly different datasets (**right**). To create the “Masked Phases” images, we follow Reichert & Serre (2014) and use the input values (and thus the fact that objects are white, and the background is black) to mask out the phase values of the background pixels. Despite achieving a reasonable reconstruction performance on all three tested datasets, the object discovery performance of our re-implementation seems to lag behind the original implementation.

- We tested a different initialization of the hidden states during evaluation, in which we randomly sampled magnitudes from a Bernoulli distribution with $p = 0.5$ and phase values from $\mathcal{U}(0, 2\pi)$.
- During evaluation, we ran the model for different numbers of iterations (100, 500, 1000), and chose the number that gave the best trade-off between performance and speed.

A.3 SlotAttention

To implement SlotAttention, we followed the description and hyperparameters provided by Locatello et al. (2020) as well as their open-source implementation¹. We used a hidden dimension of 64 throughout the model and adjusted the decoding architecture as described in Table 4 as this improved SlotAttention’s performance on our datasets. Besides this final setup that we found to perform best, we tested the following setups on the validation set of the 3Shapes dataset: the decoder setup as used by Locatello et al. (2020) for the Tetrominoes and Multi-dSprites datasets (i.e. spatially broadcast to a resolution of 32×32 and apply four transposed-convolutional layers), a setup in which the fourth transposed-convolutional layer in Table 4 is removed from the decoder, as well as a setup in which the number of channels is halved across all layers. None of these setups learned to disentangle objects on the MNIST&Shape dataset.

Table 4: Architecture used for the Spatial-Broadcast Decoder in the SlotAttention model.

Layer	Feature Dimension (H \times W \times C)	Kernel	Stride	Padding Input / Output	Activation Function
Spatial Broadcast	$4 \times 4 \times 64$	-	-	-	-
Position Embedding	$4 \times 4 \times 64$	-	-	-	-
TransConv	$7 \times 7 \times 64$	5	2	2 / 0	ReLU
TransConv	$15 \times 15 \times 64$	5	2	2 / 0	ReLU
TransConv	$32 \times 32 \times 64$	5	2	2 / 1	ReLU
TransConv	$32 \times 32 \times 64$	3	1	1 / 0	ReLU
TransConv	$32 \times 32 \times 2$	3	1	1 / 0	ReLU

A.4 Datasets

For our experiments, we generate three grayscale datasets: 2Shapes, 3Shapes, and MNIST&Shape. All images within these datasets feature a black background and white objects of differing shapes. In the 2Shapes and 3Shapes datasets, the foreground objects and the background are plain white and plain black, respectively, without noise. In the MNIST&Shape dataset, the digits exhibit differing grayscale values. All objects are placed in random locations while ensuring that no part of the object is cut-off at the image boundary.

We use four different object types (\square , \triangle , ∇ , and MNIST digits). The square has an outer side-length of 13 pixels. Both triangles are isosceles triangles, have a base-length of 17 pixels, and are 9 pixels high. Both the square’s and the triangles’ outlines have a width of 3 pixels.

For the MNIST&Shape dataset, we resize each MNIST digit to match the input image size of our dataset (i.e. 32×32) before applying it to an image. Then, we label pixels as “digit” when their value is > -0.8 after normalization to the $[-1, 1]$ range. This threshold ensures that most of the digit pixels are labeled as such, while minimizing the influence of potentially noisy background pixels. We follow the original dataset split to create the test images and divide the original training set to get 50,000 MNIST digits for our training set and 10,000 MNIST digits for our validation set.

We scale and shift all inputs to the range $[0, 1]$ for the autoencoding models, and we use an input range of $[-1, 1]$ for the SlotAttention model.

¹https://github.com/google-research/google-research/tree/master/slot_attention

B Additional Results

B.1 DBM

We test two architectures for the DBM model, 3-layer DBM and 6-layer DBM, trained for 50,000 and 100,000 steps per layer (Table 5). On the 2Shapes dataset, the 3-layer DBM trained for 100,000 steps per layer (i.e. 300,000 steps in total) achieves the best reconstruction (MSE) and object discovery (ARI-BG) performance. On the 3Shapes and MNIST&Shape datasets, the 6-layer DBM achieves the best object discovery results in terms of ARI-BG, despite creating less accurate reconstructions. In fact, for the 6-layer DBM model trained on the 3Shapes dataset, the object discovery performance in terms of ARI-BG worsens when the model is trained for longer, despite an improvement in reconstruction performance. In the main results in Table 1, we state the performance of the best model in terms of ARI-BG performance per dataset.

Table 5: MSE and ARI scores (mean \pm standard error across 8 seeds) of the two DBM models (3-layer DBM and 6-layer DBM) across the three tested multi-object datasets. On the 2Shapes dataset, the 3-layer DBM achieves the best reconstruction and object discovery performance in terms of ARI-BG, whereas the 6-layer DBM achieves better object discovery performance on the 3Shapes and MNIST&Shape dataset. Interestingly, training the 6-layer DBM model for longer on the 3Shapes dataset results in a worse object discovery performance in terms of ARI-BG despite improvements in the reconstruction performance.

Dataset	Model	Steps	MSE \downarrow	ARI+BG \uparrow	ARI-BG \uparrow
2Shapes	Complex AutoEncoder	10000	3.322e-04 \pm 1.583e-06	0.999 \pm 0.000	1.000 \pm 0.000
	3-layer DBM	150000	4.358e-03 \pm 1.068e-04	0.893 \pm 0.002	0.694 \pm 0.017
	3-layer DBM	300000	3.308e-03 \pm 1.024e-04	0.920 \pm 0.002	0.744 \pm 0.010
	6-layer DBM	300000	8.699e-03 \pm 1.442e-04	0.893 \pm 0.001	0.689 \pm 0.015
	6-layer DBM	600000	4.892e-03 \pm 5.394e-05	0.934 \pm 0.001	0.696 \pm 0.013
3Shapes	Complex AutoEncoder	100000	1.313e-04 \pm 2.020e-05	0.976 \pm 0.002	1.000 \pm 0.000
	3-layer DBM	150000	6.644e-03 \pm 1.618e-04	0.866 \pm 0.001	0.333 \pm 0.016
	3-layer DBM	300000	6.111e-03 \pm 2.530e-04	0.888 \pm 0.002	0.377 \pm 0.007
	6-layer DBM	300000	1.045e-02 \pm 1.494e-04	0.856 \pm 0.006	0.419 \pm 0.023
	6-layer DBM	600000	6.206e-03 \pm 1.058e-04	0.913 \pm 0.001	0.397 \pm 0.009
MNIST&Shape	Complex AutoEncoder	10000	3.185e-03 \pm 1.514e-04	0.783 \pm 0.004	0.971 \pm 0.011
	3-layer DBM	150000	1.381e-02 \pm 6.307e-05	0.762 \pm 0.002	0.047 \pm 0.005
	3-layer DBM	300000	1.321e-02 \pm 6.240e-05	0.755 \pm 0.001	0.065 \pm 0.008
	6-layer DBM	300000	1.839e-02 \pm 1.171e-04	0.697 \pm 0.003	0.153 \pm 0.010
	6-layer DBM	600000	1.560e-02 \pm 8.069e-05	0.718 \pm 0.002	0.175 \pm 0.006

B.2 Runtimes

To compare the training times between models, we first investigate the number of training steps that they require to achieve their best performance. For this, we plot the training curves of the Complex AutoEncoder and SlotAttention model on the 2Shapes and 3Shapes datasets in Fig. 7. In both datasets, the SlotAttention model keeps improving in performance throughout its 500,000 training steps. The Complex AutoEncoder, on the other hand, converges much faster, within 10,000 – 100,000 steps. For the DBM model, we cannot provide training curves due to its greedy layerwise training. Instead, we evaluate its performance after 50,000 and 100,000 training steps per layer in Table 5 and find that longer training times generally result in improved reconstruction performance. For the final run-time comparison, we choose the DBM model with the best ARI-BG performance per dataset.

We provide a comparison of the training times of the Complex AutoEncoder, SlotAttention and DBM model in Table 6. We find that the DBM models have the fastest training time per 10,000 steps, but are overall slower to train than the CAE due to the high number of training steps that they require. SlotAttention’s training steps are two times slower than those of the CAE, which, together with its high number of training steps, leads to significantly slower training times.

In Table 7, we compare the evaluation times of each model on the 2Shapes dataset. Since all datasets in our experiments use the same dimensionality (32×32 pixels) and contain 10,000 images, we expect these numbers to generalize well across the tested datasets. Since SlotAttention creates an explicit separation of object features into slots, its predicted object assignments are readily available

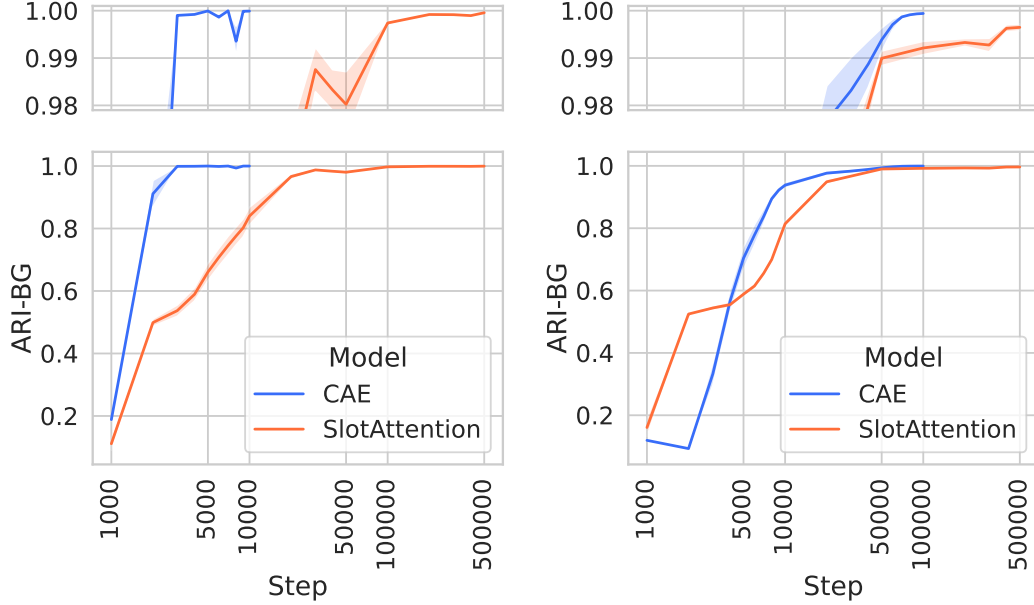


Figure 7: Training curves of the Complex AutoEncoder (CAE) and SlotAttention model (mean \pm standard error across 8 seeds) on the 2Shapes (**Left**) and 3Shapes (**Right**) dataset. We plot the ARI-BG scores on the validation set throughout training. The CAE achieves comparable or better performance within 5-50 times fewer training steps compared to the SlotAttention model.

and a single evaluation of the test set takes approximately 25.4 seconds. Both the CAE and DBM model, on the other hand, need to extract discrete object assignments from the continuous phase values using k -means, resulting in considerably longer evaluation times. While the CAE takes approximately 263.9 seconds to evaluate, due to its iterative settling procedure, the DBM takes between 520.9 and 4377.6 seconds – depending on whether we use the 3-layer or 6-layer variant.

Table 6: Training times (mean \pm standard error across 8 seeds) in terms of wall clock time for the Complex AutoEncoder, SlotAttention and DBM model across the three tested multi-object datasets. We measured the training times per 10,000 steps on the 2Shapes dataset and extrapolated the results to create a detailed and realistic break-down of training times for each dataset. This is possible, as all datasets are of the same dimensionality. For the DBM, we report the average training time per step across layers. We find that the CAE is considerably faster to train on all datasets compared to the SlotAttention and DBM model.

Dataset	Model	Steps	Training Time per 10,000 Steps (sec)	Total Training Time (min)	Relative Training Speed compared to CAE
2Shapes	Complex AutoEncoder	10000	456.6 \pm 2.5	7.6 \pm 0.0	1.0 \pm 0.0
	3-layer DBM	300000	31.5 \pm 0.2	15.7 \pm 0.1	2.1 \pm 0.0
	SlotAttention	500000	911.1 \pm 4.5	759.3 \pm 3.7	99.8 \pm 0.5
3Shapes	Complex AutoEncoder	100000	456.6 \pm 2.5	76.1 \pm 0.4	1.0 \pm 0.0
	6-layer DBM	300000	160.0 \pm 0.3	80.0 \pm 0.1	1.1 \pm 0.0
	SlotAttention	500000	911.1 \pm 4.5	759.3 \pm 3.7	10.0 \pm 0.0
MNIST&Shape	Complex AutoEncoder	10000	456.6 \pm 2.5	7.6 \pm 0.0	1.0 \pm 0.0
	6-layer DBM	600000	160.0 \pm 0.3	160.0 \pm 0.3	21.0 \pm 0.0
	SlotAttention	500000	911.1 \pm 4.5	759.3 \pm 3.7	99.8 \pm 0.5

Table 7: Evaluation times (mean \pm standard error across 8 seeds) in terms of wall clock time for the Complex AutoEncoder, SlotAttention and DBM model on the 2Shapes dataset. Since all datasets are of the same dimensionality, we expect the evaluation times on the 3Shapes and MNIST&Shape datasets to be equivalent. The SlotAttention model is the fastest to evaluate, as it immediately creates discrete object assignments. The CAE and DBM, on the other hand, require a discretization procedure with k -means leading to slower evaluation times. The DBM is further slowed down by its iterative settling procedure.

Model	Total Testing Time (sec)	Relative Testing Speed compared to CAE
Complex AutoEncoder	263.9 \pm 0.5	1.0 \pm 0.0
3-layer DBM	520.9 \pm 1.4	2.0 \pm 0.0
6-layer DBM	4377.6 \pm 4.5	16.6 \pm 0.0
SlotAttention	25.4 \pm 0.2	0.1 \pm 0.0

B.3 Sensitivity Analysis

Fig. 8 highlights the influence of the feature dimension that is output by the CAE’s encoder f_{enc} on the model’s performance. We find that the model achieves strong performance for a broad range of feature dimensions – indicating that the CAE does not require a restricted bottleneck size to create disentangled object representations.

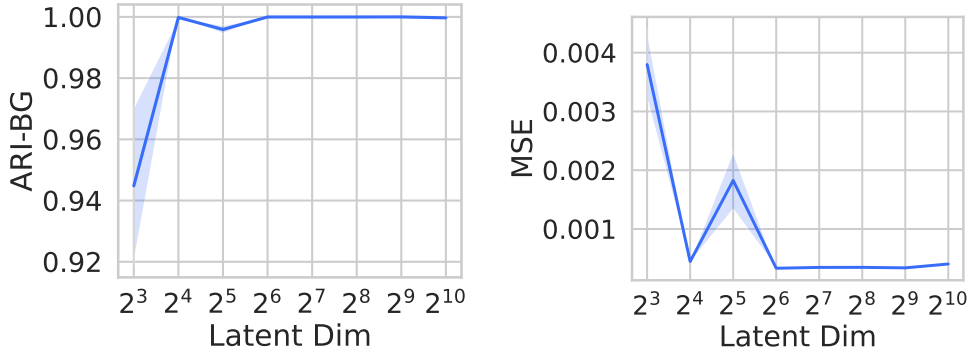


Figure 8: Influence of the latent dimension on CAE’s performance on the 2Shapes dataset (mean \pm standard error across 8 seeds). We find that the model does not require a restricted bottleneck to create disentangled object representations.

B.4 Additional Qualitative Results

We highlight the phase separations created by the Complex AutoEncoder in Fig. 9, and compare all models on the 2Shapes, 3Shapes and MNIST&Shape datasets in Figures 10, 11 and 12, respectively.

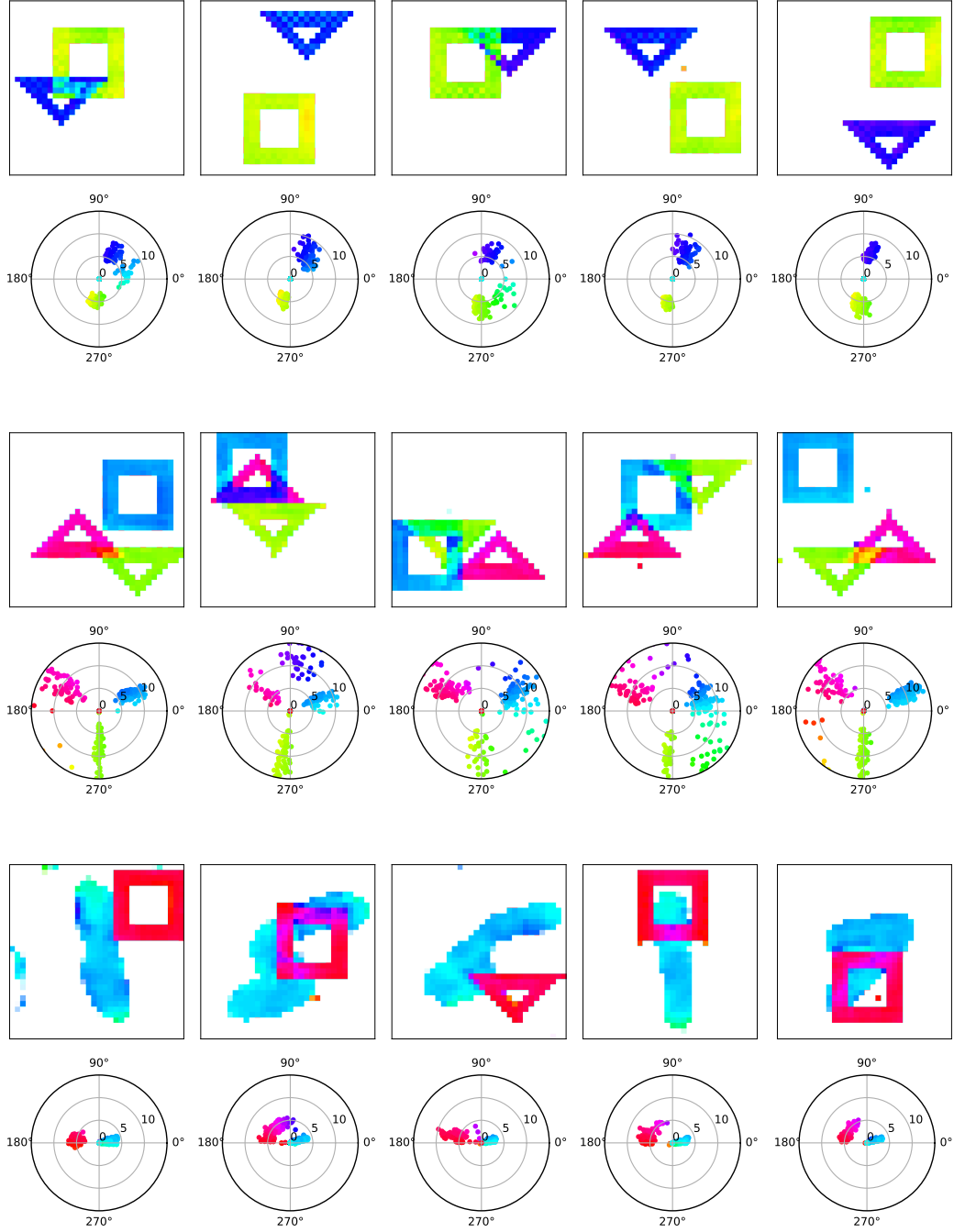


Figure 9: Phase separation in the Complex AutoEncoder on random test-samples from the 2Shapes (**Top**), 3Shapes (**Middle**) and MNIST&Shape datasets (**Bottom**). For each sample, we show the output phase images on top, and the corresponding output values in the complex plane in the bottom.

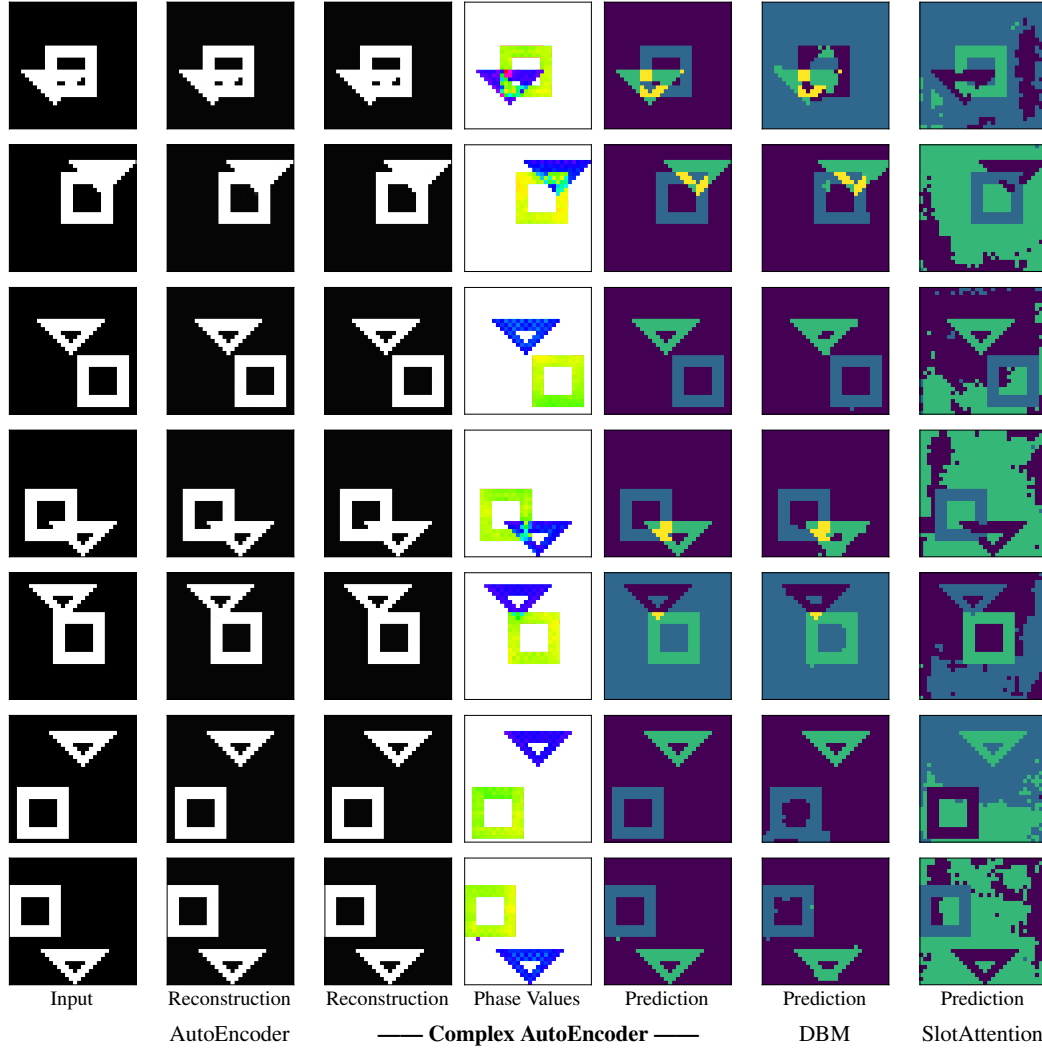


Figure 10: Visual comparison of the performance of the Complex AutoEncoder, its real-valued counterpart (AutoEncoder), the DBM model and the SlotAttention model on random test-samples from the 2Shapes dataset.

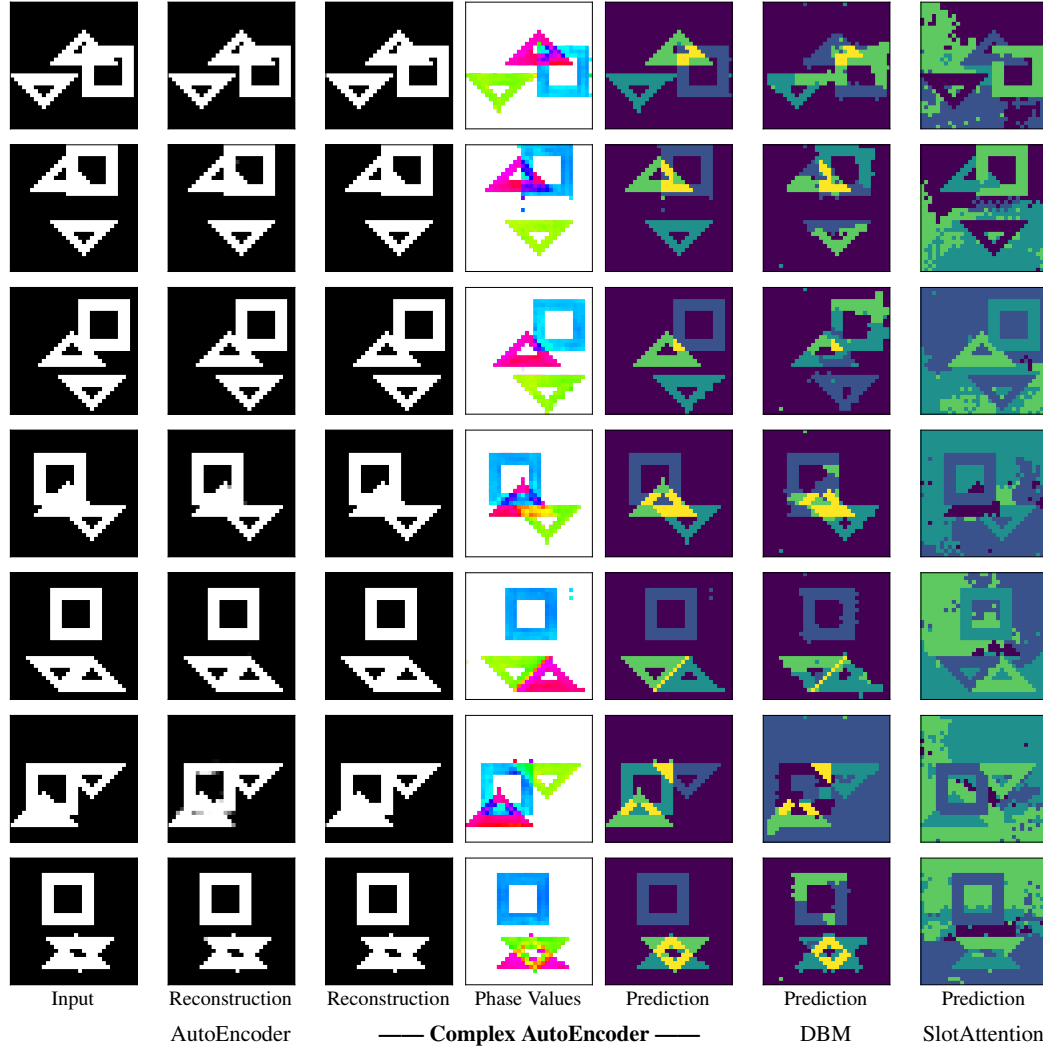


Figure 11: Visual comparison of the performance of the Complex AutoEncoder, its real-valued counterpart (AutoEncoder), the DBM model and the SlotAttention model on random test-samples from the 3Shapes dataset.

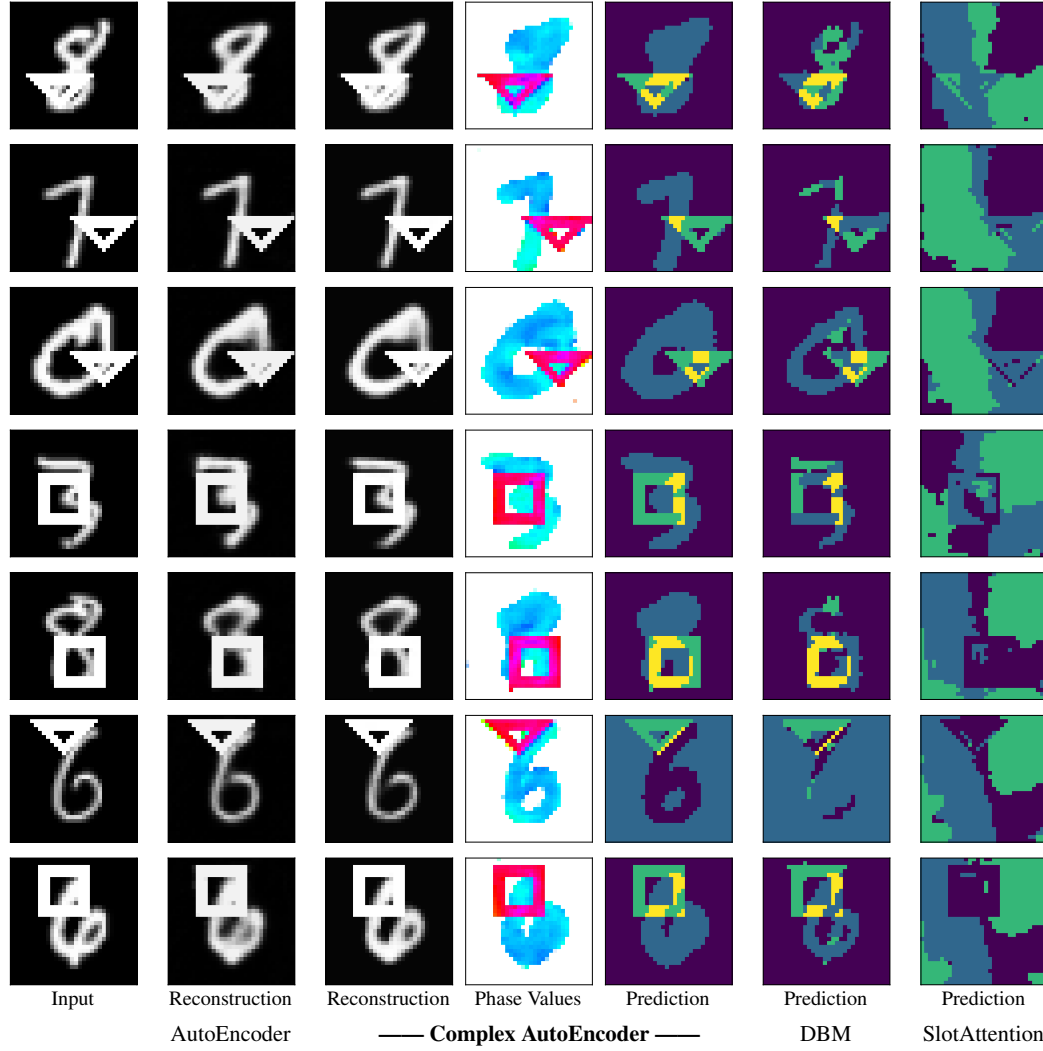


Figure 12: Visual comparison of the performance of the Complex AutoEncoder, its real-valued counterpart (AutoEncoder), the DBM model and the SlotAttention model on random test-samples from the MNIST&Shape dataset.